

## Article

# Theoretical Analysis of the Adsorption of Pentachlorophenol and 6-OH-BDE-47 (6-Hydroxy-2,2',4,4'-Tetrabromodiphenyl Ether) by Boron Nitride Nanotubes Decorated with Double-Decker Lanthanide(III) Phthalocyanine Complexes

Chien-Lin Lee, Shu-Chun Chi and Chia Ming Chang \* 

Environmental Molecular and Electromagnetic Physics (EMEP) Laboratory,  
Department of Soil and Environmental Sciences, National Chung Hsing University, Taichung 40227, Taiwan  
\* Correspondence: abinitio@dragon.nchu.edu.tw



**Citation:** Lee, C.-L.; Chi, S.-C.; Chang, C.M. Theoretical Analysis of the Adsorption of Pentachlorophenol and 6-OH-BDE-47 (6-Hydroxy-2,2',4,4'-Tetrabromodiphenyl Ether) by Boron Nitride Nanotubes Decorated with Double-Decker Lanthanide(III) Phthalocyanine Complexes. *Crystals* **2022**, *12*, 1205. <https://doi.org/10.3390/cryst12091205>

Academic Editor: Jesús Sanmartín-Matalobos

Received: 13 August 2022

Accepted: 24 August 2022

Published: 27 August 2022

**Publisher's Note:** MDPI stays neutral with regard to jurisdictional claims in published maps and institutional affiliations.



**Copyright:** © 2022 by the authors. Licensee MDPI, Basel, Switzerland. This article is an open access article distributed under the terms and conditions of the Creative Commons Attribution (CC BY) license (<https://creativecommons.org/licenses/by/4.0/>).

**Abstract:** Environmental issues have become an urgent concern, and low-cost, high-efficiency environmental remediation and energy utilization are currently high priorities. In this work, zigzag (9,0) and (18,0) boron nitride nanotubes modified by double-decker lanthanide(III) phthalocyanine complexes (BN90-LnPc<sub>2</sub>, BN180-LnPc<sub>2</sub>) were investigated by semi-empirical quantum chemistry calculations. The shorter the bond length between the nitrogen atom in the complex and the hydroxyl group of the contaminant, the greater the change in the C-O-H bond angle, implying stronger adsorption. In view of the neutral and deprotonated forms of pentachlorophenol and 6-OH-BDE-47 (6-Hydroxy-2,2',4,4'-tetrabromodiphenyl ether), the effects of the hydrogen bond on the contaminants were significantly different. The analytical results of the HSAB reactivity descriptors and frontier molecular orbitals showed that BN180-YbPc<sub>2</sub> performed best of all the composite systems, and the interaction with pentachlorophenol was stronger than with 6-OH-BDE-47. Furthermore, BN180-YbPc<sub>2</sub> is beneficial as a solar-energy material, according to its electronic excitation spectrum. Ultimately, the calculated results were as expected due to the materials' multifunctional characteristics, and the exploration of material development for specific properties will be the direction for future work.

**Keywords:** pentachlorophenol; 6-OH-BDE-47; double-decker lanthanide(III) phthalocyanine complex; boron nitride nanotube; adsorption; quantum chemistry method

## 1. Introduction

The enormous potential of boron nitride (BN) in various fields [1,2], especially the separation and purification of energy and environmental treatment, is due to its extraordinary properties, including the partial ionic characteristics of its chemical bonds and its large specific surface area [3]. As an adsorbent, it has been successfully fabricated in different morphologies through various synthesis methods, and it is highly effective at removing organic pollutants such as methylene blue (MB) and rhodamine B (RhB) [4–7]. Changing the structure of BN by adding elements or mixtures (e.g., Al, pyromellitic dianhydride) could improve its physicochemical properties, particularly its adsorption performance [8,9]. Environmental endocrine disruptors, persistent organic pollutants with strong teratogenicity, carcinogenicity, neurotoxicity, and mutagenicity, are ubiquitous. An examination of chlorinated phenols (CPs) and polybromodiphenyl ethers (PBDEs, additive brominated flame retardants) was carried out in this study. Thus, optimized BN materials were developed to make a significant contribution to environmental remediation.

Density functional theory (DFT) and molecular dynamics (MD) methods are usually aimed at investigating the adsorption between h-BN monolayers and typical aromatic organic compounds [10]. Graphene-like boron nitride (g-BN) and BN whiskers have good adsorption capacity for methylene blue (MB) and rhodamine B (RhB) via  $\pi$ - $\pi$  stacking

interactions [11,12]. A previous study revealed the binding energy, charge transfer, and electron density between armchair (5,5) boron nitride nanotubes and hydrogen halides through theoretical calculations to investigate the feasibility of BNNTs as gas sensors [13]. Subsequently, results from other studies confirmed that the reactivity with targets was increased through modification [14]. Among them, [15,16] used density functional theory calculations to investigate the interaction of pristine and X-doped ( $X = \text{Co}, \text{Fe}$ ) (8,0) single-walled boron nitride nanotubes with 2-chlorophenol (2-CP), 2,4,6-trichlorophenol (TCP), and pentachlorophenol (PCP). Since the chemical structures of PBDEs and their metabolites (hydroxylated forms, OH-BDE) are structural analogs to dioxin-like chemicals such as polychlorinated biphenyls (PCBs), dioxins (TCDD), and furans (PCDF) [17], they may induce harmful effects through similar pathways. DFT was also applied to examine the sensitivity of polychlorinated dibenzo-p-dioxin (PCDD) and polychlorinated dibenzofuran (PCDF) with pristine and decorated BNNTs [18,19]. Based on the above, we can expect that metal atoms will make adsorption on BNNTs more effective in order to eliminate or detect these pollutants. The electronic analysis and thermodynamics of adsorption in relation to PBDEs have been studied by density functional theory (DFT) and molecular dynamics (MD) methods [10,20] on boron nitride nanosheets and graphene surfaces, respectively. However, to the best of our knowledge, few theoretical studies on adsorption between BNNTs and 6-OH-BDE-47, the most abundant form of PBDE metabolite [21], have been reported.

Because of their extensive electron-conjugated systems, porphyrins and related macrocycles have been identified as promising candidates for sensors involving chromophores [22]. One kind of analogue, phthalocyanine (Pc), a highly sensitive material, is a coordination compound with electrical, light, and redox properties, and it can even be modified by incorporating control units to improve its selectivity and efficacy [23]. The spectral characteristics of this compound are tunable due to changes in the HOMO–LUMO energy level after structural changes, and this can be applied in sensors. Electrochemical and optical sensors are the most common types; they are based on the interaction between the analytes and the components, which is converted into a signal that can be processed and reported [24]. Through different transduction methods, the changes caused by the presence of other molecules can be monitored [25–29]. Phthalocyanines can also form double-decker phthalocyanine (a sandwich-type complex in which a lanthanide metal is coordinated with two phthalocyanine rings,  $\text{LnPc}_2$ ). This complex has better inherent semiconductor properties and strong electrochemical and electrochromic behavior [30], which provides a super-sensitive measuring platform for detecting specific substances (e.g., [31]). The central metal ion and substituents in the phthalocyanine ring must be taken into account, as  $\text{LnPc}_2$  is easily oxidized through the presence of electron-donating groups [30,32,33].

DFT, a powerful computational tool, is helpful for gaining an in-depth understanding of the nature of a chemical reaction from the molecular level and explaining its mechanisms. It can also reveal key information regarding the electronic properties during the adsorption process on adsorbent surfaces [34]. Currently, most geometric calculations and further studies on complicated systems are performed using density functional theory, but semi-empirical methods have emerged as good candidates for solid-phase calculations with hundreds to a few thousand atoms. Quantum chemistry methods such as DFT demand a high computational cost, and the results provided are inadequately accurate [35]. PM7/sparkle [36], a class of semi-empirical models, is a good option for the theoretical study of solid crystalline materials such as lanthanide organic frameworks (LOFs).

Boron nitride is becoming more and more popular for environmental remediation and water purification. The rational design of novel nanomaterials for clean water technologies is a solution to the impacts of natural and anthropogenic alterations on the ecosystem. In sensor development, stability and sensitivity are necessary conditions; when the boron nitride nanotube was decorated with the  $\text{LnPc}_2$  complex, the more energy released, the greater the change in the LUMO–HOMO gap, indicating that this combination was suitable for development. The objective of this study was to introduce the PM7/sparkle quantum chemistry method and HSAB descriptors to analyze the effects of larger-size  $\text{LnPc}_2$ –BNNT

complexes on two types of halogen-containing compounds in different acid–base environments and to explore the novelty and feasibility of optimized nanosensors.

## 2. Computational Details

The 3D structures of the double-decker lanthanide(III) phthalocyanine complexes Ln(III)Pc<sub>2</sub> (Ln(III) = Ce(III), Eu(III), Tb(III), and Yb(III)) were elucidated based on previous publications [37]. In order to highlight the larger difference in the lanthanoid series of chemical elements, we chose Ce(III), Eu(III), Tb(III), and Yb(III) according to the atomic number on the periodic table. Before the detailed calculations of the quantum chemistry method described below, the initial geometries of the Ln(III)Pc<sub>2</sub> were obtained by the RM1/sparkle semi-empirical Hamiltonian method [38]. Zigzag (9,0) and (18,0) boron nitride nanotube models with all the edge atoms terminated by monohydrogen were used for the following calculations. These two nanotubes with obvious size differences were primarily used to compare the effects of geometric structures on the LnPc<sub>2</sub>, so the selection of nanotubes with specific characteristics such as size and chirality was not the main goal in this study. Nanotube Modeler software (JCrystalSoft, 2018; Version 1.8) from <http://www.jcrystal.com/products/wincnt/> (accessed on 23 August 2021) was used to generate the XYZ coordinates of boron nitride nanotube models. The investigated organic pollutants included pentachlorophenol (pcp), 6-OH-BDE-47 (6ohbde47), and their deprotonated forms (pcp-H and 6ohbde47-H).

All calculations for this study were performed using MOPAC 2016 software. MOPAC 2016 is a semi-empirical quantum chemistry software [39] that is available from <http://openmopac.net> (accessed on 15 July 2021). The PM7/sparkle model in MOPAC 2016 was used to optimize the double-decker lanthanide(III) phthalocyanine complexes Ln(III)Pc<sub>2</sub> (Ln(III) = Ce(III), Eu(III), Tb(III), and Yb(III)). The geometries of all nanosystems were fully optimized using tight optimization criteria with a gradient threshold of  $4.2 \times 10^{-4}$  kJ mol<sup>-1</sup> Å<sup>-1</sup>. In order to study the role of electrostatic interaction and hydrogen bonding in the strength of the binding reaction and reveal the non-covalent intermolecular and intramolecular interactions (NCIs) [40,41], the results of the optimized geometries and Mulliken charges from PM7/sparkle were illustrated using MoCalc2012 software [40,41]. In addition, MoCalc2012 was used to draw energy level diagrams. Gabedit software was used to read AUX files calculated by MOPAC 2016 in order to visualize HOMO and LUMO [42]. The lanthanide luminescence software package (LUMPAC) was used to obtain lanthanide-containing singlet and triplet excited-state energy through INDO/S-CIS ORCA calculation [43–45].

Eight global reactivity descriptors (GAP, I, A,  $\chi$ ,  $\eta$ ,  $\mu$ , S,  $\omega$ ) were calculated according to the HOMO and LUMO energies. The highest occupied molecular orbital (HOMO) and the lowest unoccupied molecular orbital (LUMO) represent the ability of a molecule to donate and accept electrons, respectively. HOMO is subtracted from LUMO to obtain the gap (i.e., the energy gap between HOMO and LUMO). HOMO and LUMO energy values are usually applied to approximate ionization potential ( $I = -\text{HOMO}$ ) and electron affinity ( $A = -\text{LUMO}$ ) through a single easy calculation [46].

Under the framework of HSAB and conceptual density functional theory [47–50], the electron escape tendency and possibility of electron loss for a given molecular species are based on its electronic chemical potential ( $\mu$ ) and chemical hardness ( $\eta$ ). The parameters  $\mu$  and  $\eta$ , relating to the number of electrons at a constant external potential, are defined as the first and second derivatives of the energy, respectively. In the ground-state parabola model,  $\mu$  and  $\eta$  can be calculated using the ionization potential (I) and electron affinity (A). The electronegativity ( $\chi = (I + A)/2$ ), chemical hardness ( $\eta = (I - A)/2$ ), chemical potential ( $\mu = -(I + A)/2 = -\chi$ ), chemical softness ( $S = 1/2 \eta$ ), and electrophilicity index ( $\omega = \mu^2/2\eta$ ) are HSAB reactivity descriptors [51].

### 3. Results and Discussion

#### 3.1. Neutral Forms of Pentachlorophenol and 6-OH-BDE-47

##### 3.1.1. Non-Covalent Interaction (NCI)

By examining the  $\text{LnPc}_2$  decoration on the surface of the zigzag (9,0) and (18,0) boron nitride nanotubes (BN90 and BN180), we found that the color was mainly yellow and green, indicating that the force was weak. Due to the larger and flatter surface of the BN180 nanotubes, the area of non-covalent interaction was significantly larger than that of the BN90 nanotubes after  $\text{LnPc}_2$  decoration. Dispersion interactions between the outer aromatic rings of Pc led to an optimized geometry of a convex Pc structure. The results estimated by B3LYP-D (DFT-D) in [52] suggested the importance of the dispersion interactions for the structure of a Pc dimer. After the adsorption of the compounds, more blue regions were apparent between the  $\text{LnPc}_2$  complex and the pentachlorophenol (pcp), while 6-OH-BDE-47 (6ohbde47) lacked blue regions and had more repellent yellow-red areas. From the perspective of molecular morphology, phthalocyanines generally adsorb with the molecular plane parallel to the surface [53], indicating that pcp was adsorbed on the complex more stably due to its aromatic planar state (Figures 1 and 2). In addition, a light blue area appeared between the complex and the chlorine atom of pcp and the bromine atom of 6ohbde47. This was because halogen atoms have more non-bonded electrons than other atoms.

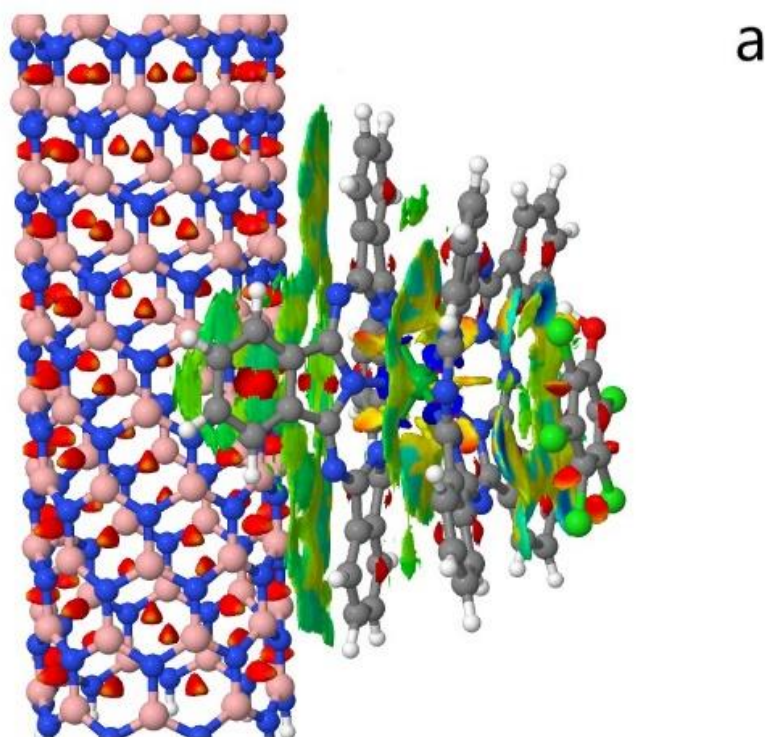
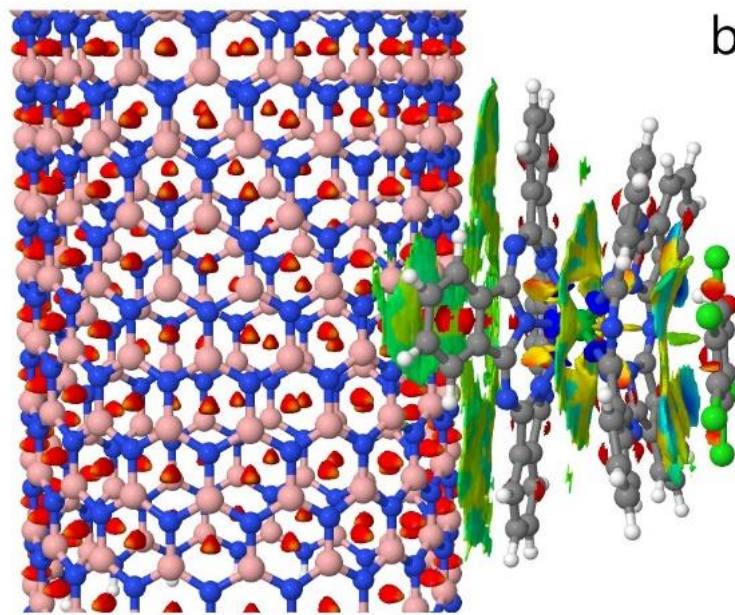
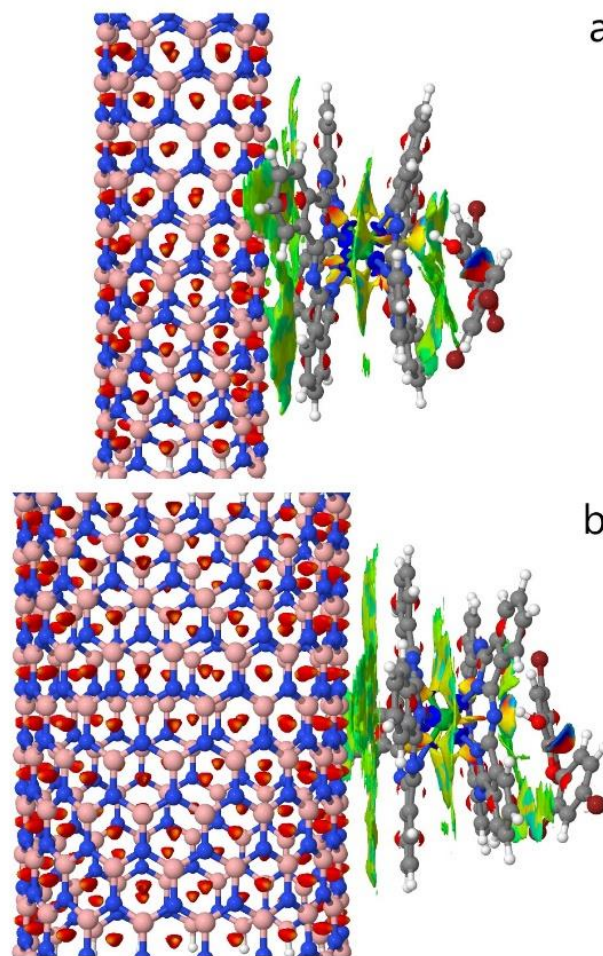


Figure 1. Cont.



**Figure 1.** Non-covalent interaction between pentachlorophenol (pcp) and zigzag (a) (9,0) and (b) (18,0) boron nitride nanotubes decorated with YbPc<sub>2</sub> complex.



**Figure 2.** Non-covalent interaction between 6-OH-BDE-47 (6ohbde47) and zigzag (a) (9,0) and (b) (18,0) boron nitride nanotubes decorated with YbPc<sub>2</sub> complex.

### 3.1.2. Reaction Enthalpy, Bond Length, and Bond Angle

The authors of [54] compared the experimental selectivity coefficient with the metal binding energy ( $\Delta E$ ), calculated by density functional theory (DFT), of the double-decker porphyrin–metal ion complex. We found that these two methods produced consistent results. According to the values of reaction enthalpy, all the adsorption reactions for the two pollutants were exothermic (Table 1). In comparison with the combined state of BN180 and BN90, the former released more energy and was relatively stable. This was consistent with [55], which found that the interaction energy between the phthalocyanine molecules and the carbon nanotubes increased with an increase in the diameter of the CNTs. The reaction enthalpy between the four complexes and BN90/BN180 was ranked as follows:  $\text{CePc}_2 < \text{EuPc}_2 < \text{TbPc}_2 < \text{YbPc}_2$ , coinciding with the order of their atomic numbers. Therefore,  $\text{YbPc}_2$  was selected for the following studies, because the  $\text{YbPc}_2$ –BN180 complex was the most stable. Regardless of the composite, as long as the contaminant was adsorbed, the energy released by the pcp was greater than that released by the 6ohbde47, which was attributed to the hydrogen bond length and bond angle.

**Table 1.** Reaction enthalpy ( $\Delta H_f$  in kcal/mol) of pentachlorophenol (pcp)/6-OH-BDE-47 (6ohbde47) adsorbed by the zigzag (9,0) and (18,0) boron nitride nanotubes decorated with  $\text{CePc}_2$ ,  $\text{EuPc}_2$ ,  $\text{TbPc}_2$ , and  $\text{YbPc}_2$  complexes.

|                         |                    |                                    | $\Delta H_f$<br>(kcal mol <sup>-1</sup> ) |                         |                    |                                    | $\Delta H_f$<br>(kcal mol <sup>-1</sup> ) |
|-------------------------|--------------------|------------------------------------|---|-------------------------|--------------------|------------------------------------|---|
| BN90                    | +CePc <sub>2</sub> | →BN90_CePc <sub>2</sub>            | −76.0                                     | BN90                    | +TbPc <sub>2</sub> | →BN90_TbPc <sub>2</sub>            | −77.8                                     |
| BN180                   | +CePc <sub>2</sub> | →BN180_CePc <sub>2</sub>           | −90.3                                     | BN180                   | +TbPc <sub>2</sub> | →BN180_TbPc <sub>2</sub>           | −93.4                                     |
| BN90_CePc <sub>2</sub>  | +pcp               | →BN90_CePc <sub>2</sub> _pcp       | −58.5                                     | BN90_TbPc <sub>2</sub>  | +pcp               | →BN90_TbPc <sub>2</sub> _pcp       | −58.4                                     |
| BN90_CePc <sub>2</sub>  | +6ohbde47          | →BN90_CePc <sub>2</sub> _6ohbde47  | −45.1                                     | BN90_TbPc <sub>2</sub>  | +6ohbde47          | →BN90_TbPc <sub>2</sub> _6ohbde47  | −45.8                                     |
| BN180_CePc <sub>2</sub> | +pcp               | →BN180_CePc <sub>2</sub> _pcp      | −57.9                                     | BN180_TbPc <sub>2</sub> | +pcp               | →BN180_TbPc <sub>2</sub> _pcp      | −58.7                                     |
| BN180_CePc <sub>2</sub> | +6ohbde47          | →BN180_CePc <sub>2</sub> _6ohbde47 | −46.0                                     | BN180_TbPc <sub>2</sub> | +6ohbde47          | →BN180_TbPc <sub>2</sub> _6ohbde47 | −45.2                                     |
| BN90                    | +EuPc <sub>2</sub> | →BN90_EuPc <sub>2</sub>            | −77.5                                     | BN90                    | +YbPc <sub>2</sub> | →BN90_YbPc <sub>2</sub>            | −79.2                                     |
| BN180                   | +EuPc <sub>2</sub> | →BN180_EuPc <sub>2</sub>           | −92.9                                     | BN180                   | +YbPc <sub>2</sub> | →BN180_YbPc <sub>2</sub>           | −94.2                                     |
| BN90_EuPc <sub>2</sub>  | +pcp               | →BN90_EuPc <sub>2</sub> _pcp       | −58.2                                     | BN90_YbPc <sub>2</sub>  | +pcp               | →BN90_YbPc <sub>2</sub> _pcp       | −57.7                                     |
| BN90_EuPc <sub>2</sub>  | +6ohbde47          | →BN90_EuPc <sub>2</sub> _6ohbde47  | −45.7                                     | BN90_YbPc <sub>2</sub>  | +6ohbde47          | →BN90_YbPc <sub>2</sub> _6ohbde47  | −45.1                                     |
| BN180_EuPc <sub>2</sub> | +pcp               | →BN180_EuPc <sub>2</sub> _pcp      | −58.5                                     | BN180_YbPc <sub>2</sub> | +pcp               | →BN180_YbPc <sub>2</sub> _pcp      | −59.0                                     |
| BN180_EuPc <sub>2</sub> | +6ohbde47          | →BN180_EuPc <sub>2</sub> _6ohbde47 | −45.5                                     | BN180_YbPc <sub>2</sub> | +6ohbde47          | →BN180_YbPc <sub>2</sub> _6ohbde47 | −45.3                                     |

The average bond lengths between the complex and BN90 were 3.69 Å and 3.69 Å, while those of the decorated BN180 were 3.73 Å and 3.75 Å, for the adsorption of pcp and 6ohbde47, respectively. When pcp/6ohbde47 was adsorbed onto any composite system, the distance between the complex and the BNNT surface did not show a significant change. The original C–O–H angles of pcp and 6ohbde47 were 113.27° and 111.94°, respectively. After adsorption by LnPc<sub>2</sub>–BNNTs, both bond angles decreased (from 113.27° to 109.7° and 108.5° and from 111.94° to 111.3° and 111.2°). For pcp, the change in C–O–H bond angle was greater than that for 6ohbde47, which was related to the planar structure of pcp (Figures 3 and 4). We also found that when BN180 adsorbed pentachlorophenol, the hydrogen bond distance between the complex and the pcp was significantly shortened by 0.34 Å (from 2.58 Å to 2.24 Å), resulting in greater deformation of the hydroxyl group, i.e., the adsorption effect of BN180 was stronger. On the other hand, because the adsorption surface area of BN90 was smaller than that of BN180, the surface binding of BN90 caused the heterocyclic structure of the YbPc<sub>2</sub> complex to bend (Figures 3 and 4). This was also one of the reasons why the adsorption structure of the BN90 composite system was more unstable than that of the BN180 system when adsorbing pcp/6ohbde47. According to the density functional theory (DFT) calculations, the Pc moiety in the lanthanide diphthalocyanine complex and the trifluoroacetic acid (TFA) generated a conjugate through a moderate-strength hydrogen bond (>N··H··) [56]. The hydrogen bond donor was the oxygen in

the TFA carboxylic acid, which formed a hydrogen bond with the nitrogen in the LnPc<sub>2</sub> macrocycle, in agreement with the results of this study.

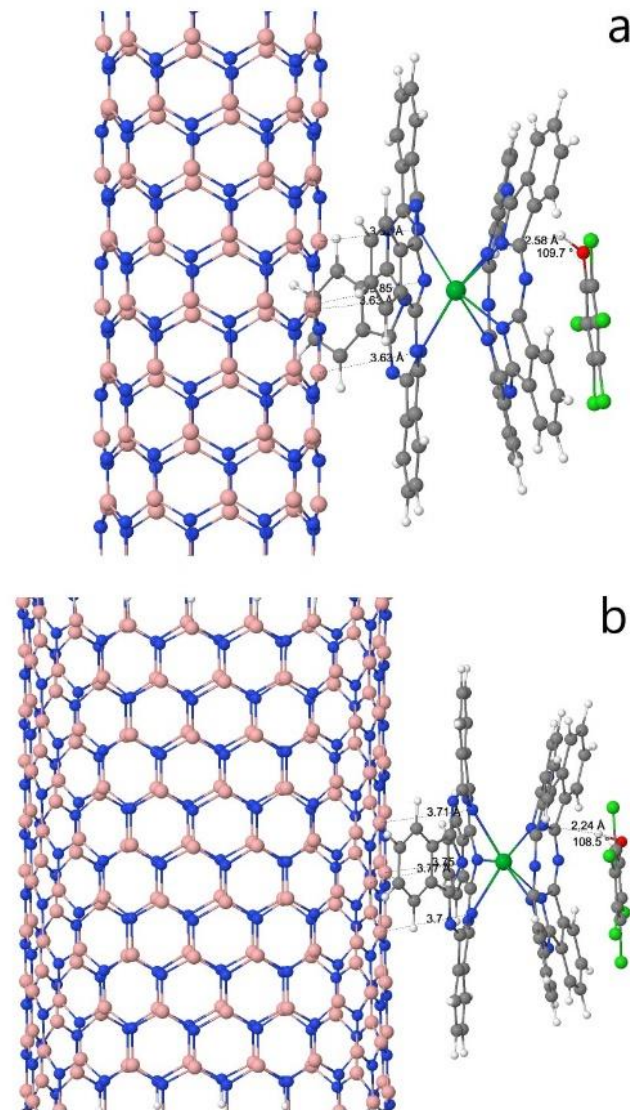


**Figure 3.** Equilibrium structures of pentachlorophenol (pcp) adsorbed on the zigzag (a) (9,0) and (b) (18,0) boron nitride nanotubes decorated with YbPc<sub>2</sub> complex.

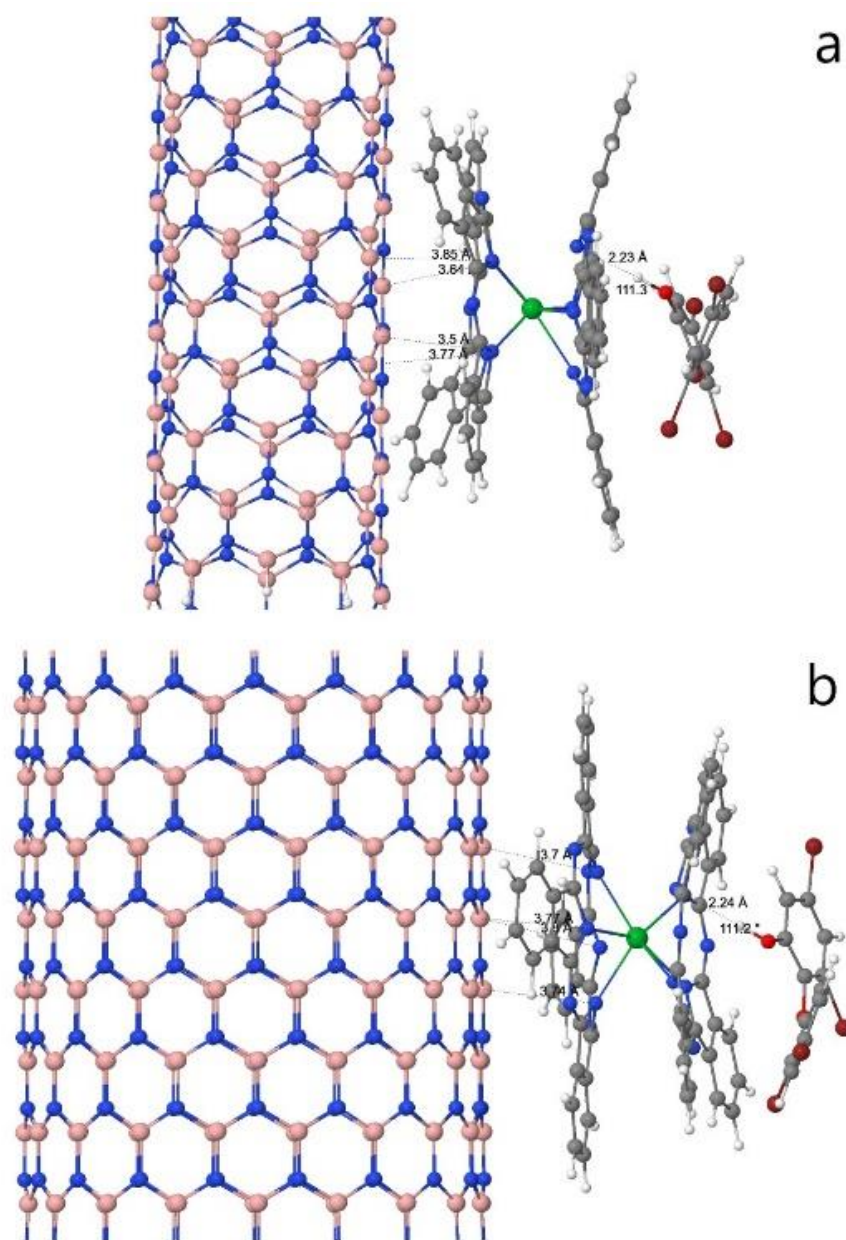


**Figure 4.** Equilibrium structures of 6-OH-BDE-47 (6ohbde47) adsorbed on the zigzag (a) (9,0) and (b) (18,0) boron nitride nanotubes decorated with YbPc<sub>2</sub> complex.

### 3.2. Deprotonated Forms of Pentachlorophenol and 6-OH-BDE-47

#### 3.2.1. Non-Covalent Interaction (NCI)

The color distribution of the decorated BNNT surfaces was similar to the results described for the neutral forms. However, when the pcp/6ohbde47 was deprotonated, the NCI between the contaminant and the complex was quite different, especially in the red area. As shown in the figure, the blue region of the pcp/6ohbde47 with hydrogen bonds generally covered larger and wider areas than that without hydrogen atoms after deprotonation. When using BN90 and BN180, the former presented a light blue area between the pcp-H and the complex and a small area of yellow-green, and the latter presented a smaller blue area and covered more yellow-green. Conversely, 6ohbde47-H exhibited more yellow and red areas and lacked blue areas, indicating that pcp-H was the most attractive option (Supplementary data Figures S1 and S2).

### 3.2.2. Reaction Enthalpy, Bond Length, and Bond Angle

According to Supplementary Materials Table S1, the adsorption of pcp-H by the BN90 nanotubes decorated with any complex was an exothermic reaction, and the order of exothermic magnitude was  $\text{CePc}_2 > \text{EuPc}_2 > \text{TbPc}_2 > \text{YbPc}_2$ . The rest of the components were all endothermic, and the sequence showed that  $\text{YbPc}_2$  had the most and  $\text{CePc}_2$  the least magnitude. Compared with the neutral forms of pcp/6ohbde47, the stability of pcp-H/6ohbde47-H adsorbed by the decorated BNNTs was significantly decreased. Additionally, in terms of removing pollutants, only pcp-H was effectively adsorbed by the BN90 complexes.

After deprotonation, the distance between the complex and the pcp-H/6ohbde47-H was greater than before deprotonation, and the adsorption structure was more unstable. Based on the above results, the influence of the hydrogen bonding interactions was confirmed. Once a hydrogen bond was created in the neutral forms, the dispersion between the complex and the contaminant increased, resulting in a stronger interaction than in the deprotonated forms (Supplementary Materials Figures S3 and S4).

### 3.3. The Frontier Molecular Orbital (FMO)

In the molecular orbital diagram, the orbital lobes of the HOMO in BN90 and BN180 were mainly concentrated at the end of the nitrogen–hydrogen bonds, and the color reflected the phase of the wave function. The orbital lobe moved toward the ends of the nitrogen because nitrogen has a higher electronegativity than boron. As for the LUMO diagram, the orbital lobes were concentrated at the end of the borohydride bonds. The nitrogen–boron bonds of the HOMO were exposed, while the LUMO orbital lobes were densely covered, especially the LUMO of BN180. After the nanotubes were modified with complexes, as shown in Figure 5, the HOMO was distributed on the  $\text{LnPc}_2$ , while the boron nitride nanotubes were occupied by the LUMO, indicating that the complex was an electron donor. The LUMO difference between the BN90– $\text{YbPc}_2$  and BN180– $\text{YbPc}_2$  complexes was very small, but we could still observe that the latter had a larger distribution range. However, the HOMO varied significantly. The complex was attached to the BN180 surface more closely, and the stronger interaction was consistent with the reaction enthalpy.

The greater the gap between the HOMO and LUMO, the more difficult it is for electron transition to occur. This kind of molecule cannot easily be polarized, and its stability is relatively high. BN180 (HOMO:  $-7.846$  eV, LUMO:  $-1.913$  eV) had a gap of  $5.933$  eV and a higher stability than BN90 (HOMO:  $-7.781$  eV, LUMO:  $-1.893$  eV). When the BNNTs were modified by  $\text{LnPc}_2$ , the energy gap of the BN180– $\text{YbPc}_2$  varied greatly (the HOMO increased by  $3.273$  eV, and the LUMO increased by  $0.987$  eV). The gap was reduced to  $3.647$  eV (HOMO:  $-4.533$  eV, LUMO:  $-0.508$  eV for BN90– $\text{YbPc}_2$ ), and the reactivity was improved, that is, the nanotubes had high sensitivity and lower qualitative and quantitative errors as a sensor.

Single-molecule magnets (SMM) have broad application prospects in sensors. As double-decker Pc complexes with lanthanoid metal ions show single-molecule magnet behavior, they have attracted much attention [57]. Nanomagnetic particles exhibit certain quantum behaviors that allow single-molecule magnets to substantially enhance information storage, which means that  $\text{LnPc}_2$ -formed devices have stronger data storage capacities [58].

Previous studies have shown that the terbium(III) bis-phthalocyaninato complex,  $\text{TbPc}_2$ , maintains its SMM behavior at up to  $9$  K on a graphene/SiC(0001) substrate, which is highly promising for molecular spintronic applications [59]. Low-temperature scanning tunneling microscopy and spectroscopy were employed by Candini et al. to investigate double-decker  $\text{DyPc}_2$  molecules adsorbed on Au(111). The experimental results revealed that the Dy atoms barely contributed to the tunneling current, that is, the  $4f$  states in the double-decker  $\text{DyPc}_2$  molecule were inaccessible [60]. This is intriguing for applications in nanoscale data storage or quantum computing with stable features in terms of the surface adsorbed by single-molecule magnets. Previous results obtained using density functional theory showed that molecules are only weakly adsorbed on magnesium oxide

and silver. The enhanced magnetic stability of DyPc<sub>2</sub> on oxide film, in conjunction with previous experiments on the TbPc<sub>2</sub> analogue, points to the stabilization effect induced by magnesium oxide [61].

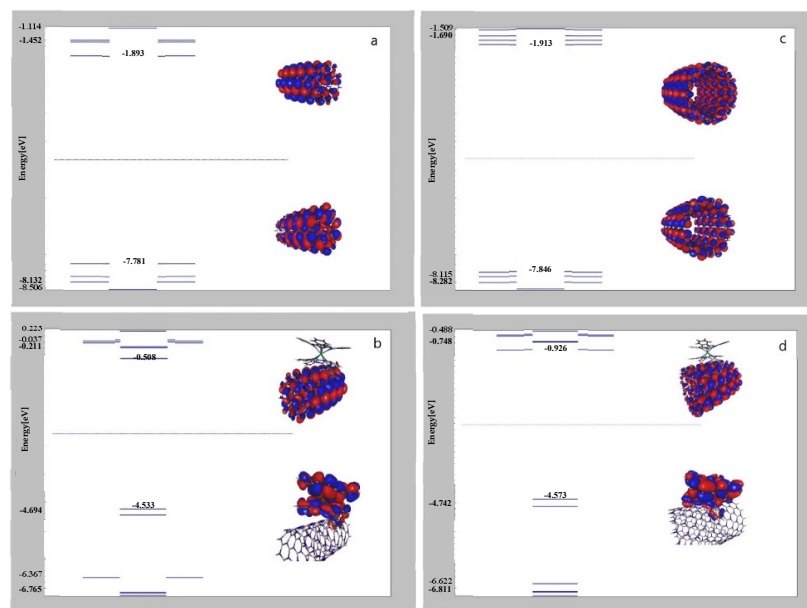


**Figure 5.** Energy level diagrams and frontier molecular orbitals (HOMO and LUMO): (a) zigzag (9,0) boron nitride nanotubes and (b) zigzag (9,0) boron nitride nanotubes decorated with YbPc<sub>2</sub> complex; (c) zigzag (18,0) boron nitride nanotubes and (d) zigzag (18,0) boron nitride nanotubes decorated with YbPc<sub>2</sub> complex.

### 3.4. The Electronic Excitation Spectrum

Except for YbPc<sub>2</sub>, the maximum wavelength ( $\lambda_{\text{max}}$ ) of the other complexes and decorative nanotubes was about 640 nm (visible range), which may boost the electron transfer in photoconducting electronic components. In particular, owing to the large conjugated electron system in phthalocyanine, its porphyrin units have intense absorption bands in the 400–450 nm ( $\pi$ – $\pi^*$  transition) and 500–700 nm regions [53]. Rich redox chemistry as well as photoinduced electron transfer are necessary for efficient photon harvesting to make the most of the solar photon flux, and macrocycles such as phthalocyanine have achieved these physical properties [62]. After BN90 was modified with CePc<sub>2</sub>, the wavelength of the spectrum was slightly blue-shifted (Figure 6a,b). When EuPc<sub>2</sub>, TbPc<sub>2</sub>, and YbPc<sub>2</sub> were used to modify BN90, the spectral wavelengths all showed a red shift. In fact, due to the close atomic numbers, the electronic excitation spectrum of EuPc<sub>2</sub> was similar to that of TbPc<sub>2</sub> (Figure 6c–f). After combination with BN90, the area of the peak (especially the largest peak) of YbPc<sub>2</sub> increased slightly (Figure 6g,h).

In summary, except for CePc<sub>2</sub>, the spectra exhibited a red-shift phenomenon, which also meant that the distance between the ground state and the excited state decreased, the excitation energy of the nanohybrid system was reduced, and the wavelength increased. The ultraviolet–visible (UV–Vis) absorption spectra revealed a reduction in the energy bandgap to enhance the visible-light absorption during surface modification [63]. LnPc<sub>2</sub> is easily oxidized by the presence of electron-donating groups when it develops in lanthanides [30,32,33]. The authors of [64] pointed out that TbPc<sub>2</sub> can be used as a material that photochemically interacts with volatile organic compounds (VOC) in real time. The electronic absorption spectrum also changes with the oxidation state, and the color change from green to blue or red can be observed with the naked eye. Therefore, if a nanosystem with composite materials is used in a sensor, solar energy can be converted into electrical energy to solve the charging problem.

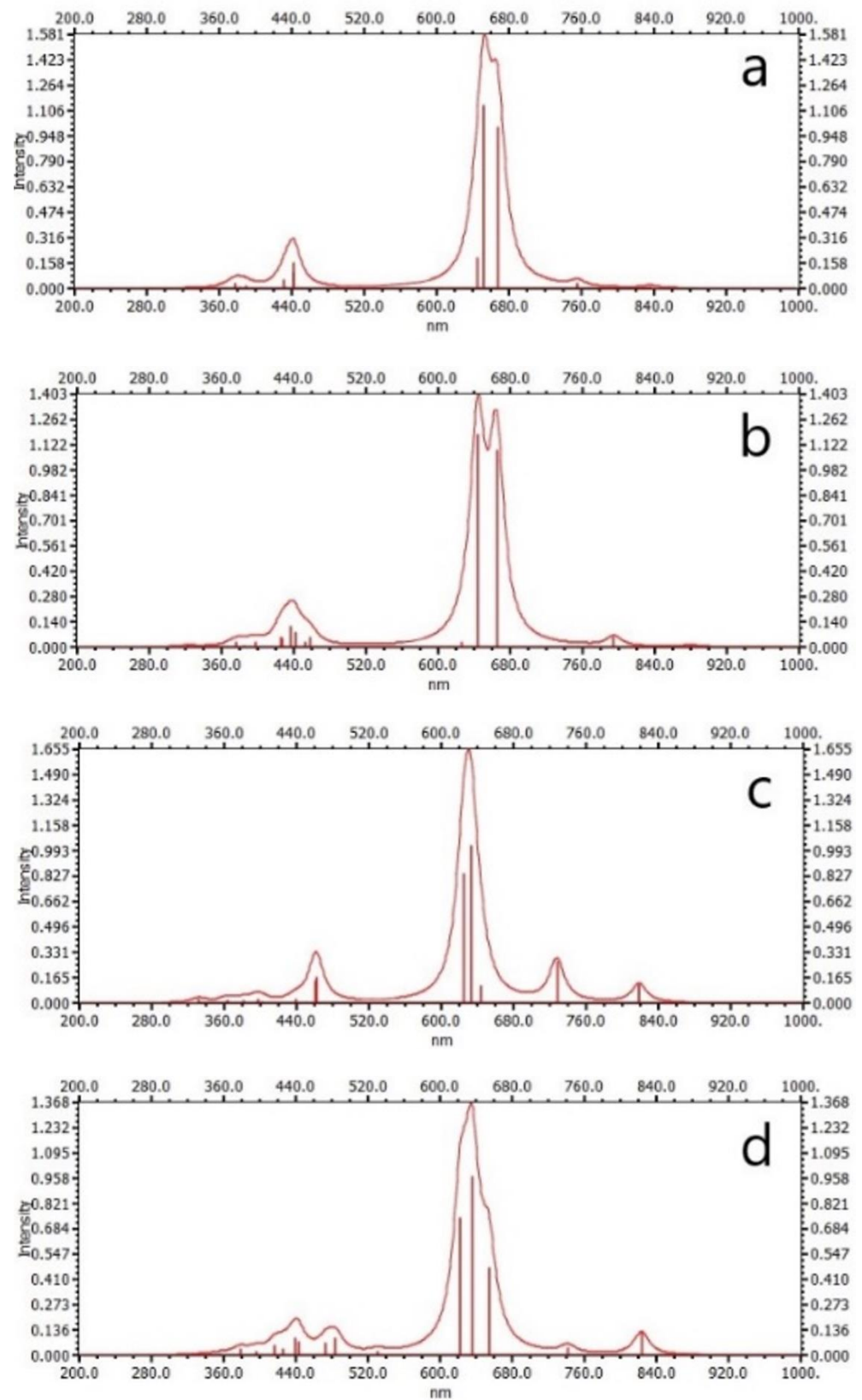
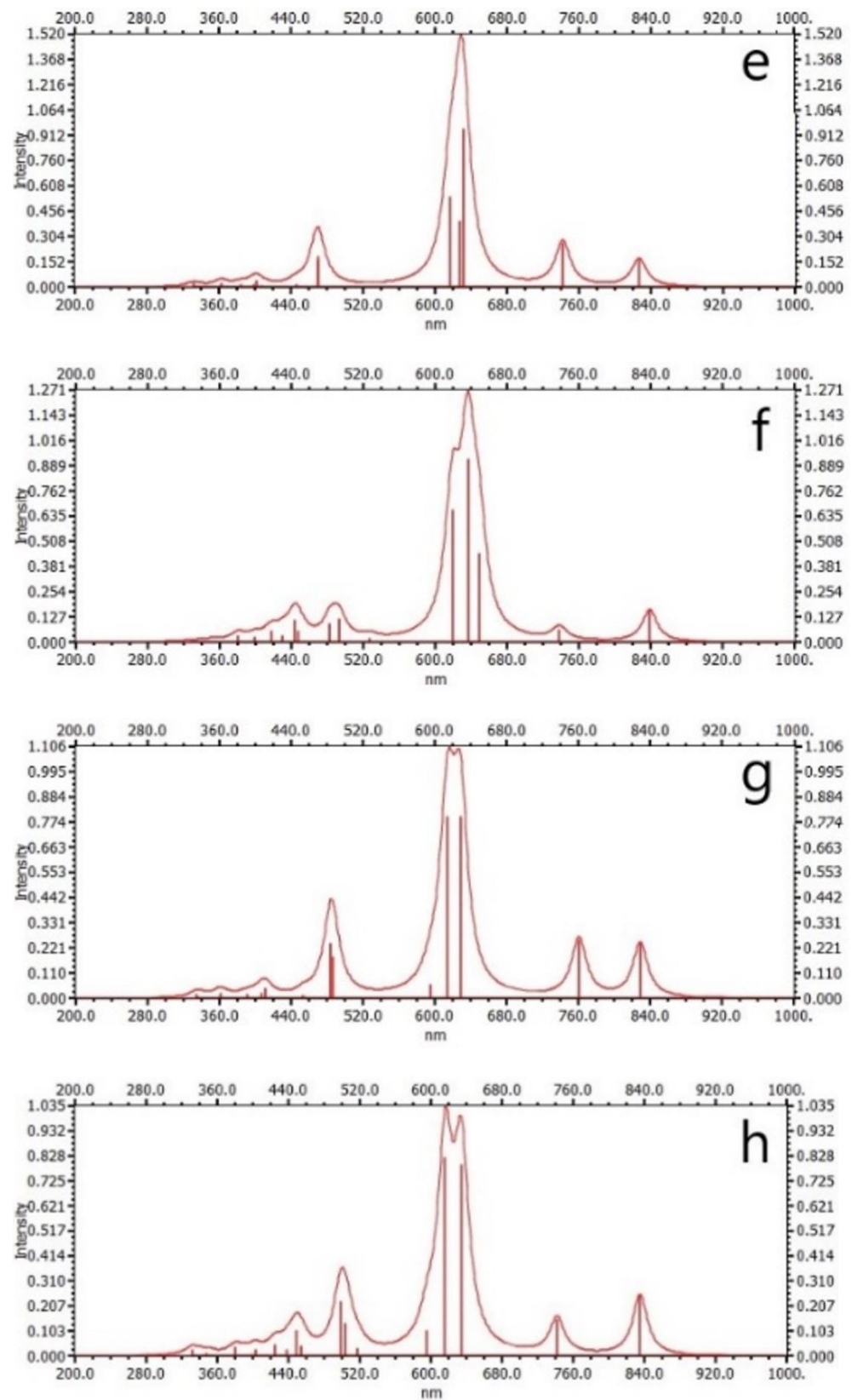


Figure 6. Cont.



**Figure 6.** Electronic excitation spectra: (a)  $CePc_2$ , (b) zigzag (9,0) boron nitride nanotubes decorated with  $CePc_2$  complex, (c)  $EuPc_2$ , (d) zigzag (9,0) boron nitride nanotubes decorated with  $EuPc_2$  complex, (e)  $TbPc_2$ , (f) zigzag (9,0) boron nitride nanotubes decorated with  $TbPc_2$  complex, (g)  $YbPc_2$ , and (h) zigzag (9,0) boron nitride nanotubes decorated with  $YbPc_2$  complex.

### 3.5. Hard and Soft Acid and Base (HSAB) Theoretical Analysis

The eight descriptors summarized in Table 2 indicate that the value of BN180 was slightly greater than the value of BN90, except for the chemical softness  $S$  and the chemical potential  $\mu$ . Except for  $S$  and  $\mu$ , the descriptors all decreased after the modification of the BNNTs, showing that improvement occurred. Among them, the BN180 complex had a particularly strong effect on reducing the chemical hardness and gap value to promote the reactivity of BN180. As shown in Table 2, regardless of the type of pollutant, deprotonation caused all the descriptor values to decrease (except for  $S$  and  $\mu$ ).

**Table 2.** HSAB reactivity descriptors in the present study.

|                         | GAP (eV) | I (eV) | A (eV) | $\chi$ (eV) | $\eta$ (eV) | $\mu$ (eV) | $S$ (eV <sup>-1</sup> ) | $\omega$ (eV) |
|-------------------------|----------|--------|--------|-------------|-------------|------------|-------------------------|---------------|
| CePc <sub>2</sub>       | 4.858    | 4.544  | -0.314 | 2.115       | 2.429       | -2.115     | 0.206                   | 0.921         |
| EuPc <sub>2</sub>       | 4.813    | 4.456  | -0.357 | 2.050       | 2.407       | -2.050     | 0.208                   | 0.873         |
| TbPc <sub>2</sub>       | 4.798    | 4.423  | -0.375 | 2.024       | 2.399       | -2.024     | 0.208                   | 0.854         |
| YbPc <sub>2</sub>       | 4.783    | 4.380  | -0.403 | 1.989       | 2.392       | -1.989     | 0.209                   | 0.827         |
| BN90                    | 5.888    | 7.781  | 1.893  | 4.837       | 2.944       | -4.837     | 0.170                   | 3.974         |
| BN180                   | 5.933    | 7.846  | 1.913  | 4.880       | 2.967       | -4.880     | 0.169                   | 4.013         |
| BN90-CePc <sub>2</sub>  | 4.093    | 4.654  | 0.561  | 2.608       | 2.047       | -2.608     | 0.244                   | 1.661         |
| BN90-EuPc <sub>2</sub>  | 4.050    | 4.585  | 0.535  | 2.560       | 2.025       | -2.560     | 0.247                   | 1.618         |
| BN90-TbPc <sub>2</sub>  | 4.029    | 4.560  | 0.531  | 2.546       | 2.015       | -2.546     | 0.248                   | 1.608         |
| BN90-YbPc <sub>2</sub>  | 4.025    | 4.533  | 0.508  | 2.521       | 2.013       | -2.521     | 0.248                   | 1.578         |
| BN180-CePc <sub>2</sub> | 3.749    | 4.698  | 0.949  | 2.824       | 1.875       | -2.824     | 0.267                   | 2.126         |
| BN180-EuPc <sub>2</sub> | 3.706    | 4.636  | 0.930  | 2.783       | 1.853       | -2.783     | 0.270                   | 2.090         |
| BN180-TbPc <sub>2</sub> | 3.681    | 4.609  | 0.928  | 2.769       | 1.841       | -2.769     | 0.272                   | 2.082         |
| BN180-YbPc <sub>2</sub> | 3.647    | 4.573  | 0.926  | 2.750       | 1.824       | -2.750     | 0.274                   | 2.073         |
| pcp                     | 8.301    | 9.811  | 1.510  | 5.661       | 4.151       | -5.661     | 0.120                   | 3.860         |
| 6ohbde47                | 8.382    | 9.278  | 0.896  | 5.087       | 4.191       | -5.087     | 0.119                   | 3.087         |
| pcp-H                   | 7.840    | 4.793  | -3.047 | 0.873       | 3.920       | -0.873     | 0.128                   | 0.097         |
| 6ohbde47-H              | 6.987    | 4.638  | -2.349 | 1.145       | 3.494       | -1.145     | 0.143                   | 0.187         |

The energy gap changes greatly during a reaction and can be used as an indicator of the applicability of a sensor material. The gap order was CePc<sub>2</sub> > EuPc<sub>2</sub> > TbPc<sub>2</sub> > YbPc<sub>2</sub>. BNNTs are an electrical insulator with a bandgap of ~5.5 eV, as determined by [65–67]. For these two types of nanotubes, it was found that BN180 > BN90, with the larger radius of BN180 being due to the curvature effect [68]. The overlap of  $\pi$ -orbitals in each ring resulted in a narrow energy gap [69]. However, drastic distortion would reduce the electron transport capacity. Thus, the band gap of the BN180 complex was smaller. The gap value of the BN180 complex decreased the most, especially when Ln = Yb. From a comprehensive point of view, the gap value is positively correlated with chemical hardness, so BN180–YbPc<sub>2</sub> was found to be the most suitable alternative for sensor development in this work as it had the highest stability. The order of ionization energy was CePc<sub>2</sub> > EuPc<sub>2</sub> > TbPc<sub>2</sub> > YbPc<sub>2</sub>, and the ionization energy of BN180 was greater than that of BN90. In terms of electron affinity, that of BN180 was greater than that of BN90. After the BNNTs were decorated, the electron affinity decreased. In general, the results of the ionization energy and electron affinity were in good agreement with each other. On the other hand, it was difficult for the deprotonated compounds (anions) to obtain electrons, and the electron affinity was reduced.

The order of electronegativity was CePc<sub>2</sub> > EuPc<sub>2</sub> > TbPc<sub>2</sub> > YbPc<sub>2</sub>, implying that YbPc<sub>2</sub> had a weaker attraction to electrons. The electronegativity of BN180 was greater than that of BN90. Regarding the difference between the BNNTs and the complexes, the difference between BN180 and YbPc<sub>2</sub> was the largest. Therefore, BN180–YbPc<sub>2</sub> had a strong electron donor–acceptor interaction, resulting in the highest reaction enthalpy (Table 1), and this BN180–YbPc<sub>2</sub> relationship was almost identical to the Pc nanostructure (fullerene, carbon nanotubes) [70]. The pcp had a higher electronegativity than the 6ohbde47 because it has more chlorine atoms, which have a greater electronegativity than bromine atoms. As for the deprotonation state,  $\chi$  was significantly reduced, which was not conducive to

attracting electrons; this was clearly indicated by the electron affinity, with pcp-H having a much lower value than 6ohbde47-H. The greater the chemical hardness, the greater the resistance to charge redistribution, and the more difficult polarization became. It can be observed that  $CePc_2 > EuPc_2 > TbPc_2 > YbPc_2$  in the  $\eta$  column, and  $BN180 > BN90$ . The chemical hardness value of the BNNTs decreased significantly after modification, and the variation in that of BN180 was greater than in that of BN90, indicating that both polarization and reactivity increased.

The parameter  $\mu$  represents the negative value of electronegativity. Among the four complexes,  $YbPc_2$  had the largest chemical potential. A comparison of the two types of nanotubes exhibited that the chemical potential of BN90 was greater than that of BN180, indicating that BN180 was a better electron acceptor. The difference between  $YbPc_2$  and BN180 was strengthened by the electronegativity, as electrons could easily flow from the  $YbPc_2$  to the BN180. The order of chemical potential was  $pcp-H > 6ohbde47-H > 6ohbde47 > pcp$ , indicating that the first two pollutants were repelled from accepting electrons. When the two nanotubes were decorated with the complexes, the chemical potential tended to increase, and increasing the chemical potential difference between the nanotubes and the contaminant promoted the transfer of electrons.  $BN180-YbPc_2$  and pcp comprised the most compatible system. Contrary to  $\eta$ , the larger the value of  $S$ , the lower the charge density, and the easier polarization became. Polarization enhanced the reactivity of the molecules involved in the decoration of the complex. The chemical softness of  $BN180-YbPc_2$  reached as high as 0.274, which was the maximum value and showed the preferability of pcp compared to 6ohbde47 in the neutral forms of the molecules. We found that the chemical softness of 6ohbde47-H was greater, mainly because the molecular volume of 6ohbde47-H was larger. The larger the value of the electrophilicity index, the more suitable a substance is as an electrophilic reagent in chemical reactions. The order was  $CePc_2 > EuPc_2 > TbPc_2 > YbPc_2$ , and the electrophilicity index of BN180 was greater than that of BN90, which was similar to the electronegativity results.

Finally, we should emphasize that the main purpose of this article was to discuss the potential application of nanosensors. Thus, nanotubes with obvious size differences were primarily used to compare the trends of the geometric effects on  $LnPc_2$ . Modified nanotubes with specific characteristics (e.g., radius, chirality, number of tube walls) that exhibit the best performance could be the next research goal and deserve careful scrutiny in future studies.

#### 4. Conclusions

The semi-empirical PM7 quantum chemistry method was used to calculate the equilibrium structures and electronic properties of BNNTs, complexes, and organic pollutants. The HSAB descriptors helped us understand the intermolecular interactions in detail. In terms of electron donor–acceptor relationships, boron nitride nanotubes showed good electron acceptability. Modification with the electron donor  $YbPc_2$  to form a stable structure made BN180 easily polarized sensing material with a higher electronic transition. The results of the non-covalent interactions and adsorption enthalpy showed that when  $BN180-YbPc_2$  is applied in sensors, it is most suitable for pcp adsorption due to the hydrogen bonds, followed by 6ohbde47. If the contaminant is deprotonated in an alkaline environment, the reaction enthalpy decreases and the monitoring efficiency is reduced. Last but not least, since the absorption spectrum of  $BN180-YbPc_2$  is concentrated in the visible range, it is helpful for the energy conversion aspect of solar energy applications. The use of solar materials would simultaneously solve the problems of time-consuming and energy-intensive environmental remediation. Overall, the use of materials with high energy conversion and high selectivity for the removal of environmental pollutants would be economical and provide the best of both worlds. Therefore, this theoretical analysis can be used as a future guide for predicting material prospects in diverse applications in order to save on experimental costs.

**Supplementary Materials:** The following supporting information can be downloaded at: <https://www.mdpi.com/article/10.3390/cryst12091205/s1>.

**Author Contributions:** Conceptualization, C.-L.L., S.-C.C. and C.M.C.; methodology, C.-L.L., S.-C.C. and C.M.C.; software, C.-L.L., S.-C.C.; validation, C.M.C.; formal analysis, C.-L.L., S.-C.C. and C.M.C.; investigation, C.-L.L.; resources, C.M.C.; data curation, C.-L.L.; writing—original draft preparation, C.-L.L.; writing—review and editing, C.M.C.; visualization, C.-L.L., S.-C.C. and C.M.C.; supervision, C.M.C.; project administration, C.M.C.; funding acquisition, C.M.C. All authors have read and agreed to the published version of the manuscript.

**Funding:** This research was funded by the National Science Council of Taiwan, Republic of China and grant number [MOST 111-2321-B-005-004].

**Institutional Review Board Statement:** Not applicable.

**Informed Consent Statement:** Not applicable.

**Data Availability Statement:** Not applicable.

**Acknowledgments:** The authors thank the National Science Council of Taiwan, Republic of China, MOST 111-2321-B-005-004 for providing financial support. Computer time was provided by the National Center for High-Performance Computing.

**Conflicts of Interest:** The authors declare no conflict of interest.

## References

1. Yoosefian, M.; Mirhaji, E.; Afshar, M.; Juan, A. Molecular dynamics simulations on interaction of ssDNA-causing DM1 with carbon and boron nitride nanotubes to inhibit the formation of CTG repeat secondary structures. *Appl. Surf. Sci.* **2020**, *524*, 146572. [CrossRef]
2. Mirhaji, E.; Afshar, M.; Rezvani, S.; Yoosefian, M. Boron nitride nanotubes as a nanotransporter for anti-cancer docetaxel drug in water/ethanol solution. *J. Mol. Liq.* **2018**, *271*, 151–156. [CrossRef]
3. Xiong, J.; Di, J.; Zhu, W.; Li, H. Hexagonal boron nitride adsorbent: Synthesis, performance tailoring and applications. *J. Energy Chem.* **2020**, *40*, 99–111. [CrossRef]
4. Xue, L.; Lu, B.; Wu, Z.-S.; Ge, C.; Wang, P.; Zhang, R.; Zhang, X.-D. Synthesis of mesoporous hexagonal boron nitride fibers with high surface area for efficient removal of organic pollutants. *Chem. Eng. J.* **2014**, *243*, 494–499. [CrossRef]
5. Zhang, X.; Lian, G.; Zhang, S.; Cui, D.; Wang, Q. Boron nitride nanocarpet: Controllable synthesis and their adsorption performance to organic pollutants. *CrystEngComm* **2012**, *14*, 4670–4676. [CrossRef]
6. Maiti, K.; Thanh, T.D.; Sharma, K.; Hui, D.; Kim, N.H.; Lee, J.H. Highly efficient adsorbent based on novel cotton flower-like porous boron nitride for organic pollutant removal. *Compos. Part B Eng.* **2017**, *123*, 45–54. [CrossRef]
7. Singla, P.; Goel, N.; Kumar, V.; Singhal, S. Boron nitride nanomaterials with different morphologies: Synthesis, characterization and efficient application in dye adsorption. *Ceram. Int.* **2015**, *41*, 10565–10577. [CrossRef]
8. Song, Q.; Fang, Y.; Wang, J.; Liang, J.; Hu, Q.; Liu, Z.; Huang, Y.; Xue, Y.; Lin, J.; Tang, C. Enhanced adsorption of fluoride on Al-modified boron nitride nanosheets from aqueous solution. *J. Alloy Compd.* **2019**, *793*, 512–518. [CrossRef]
9. Guo, Y.; Wang, R.; Yan, C.; Wang, P.; Rao, L.; Wang, C. Developing boron nitride-pyromellitic dianhydride composite for removal of aromatic pollutants from wastewater via adsorption and photodegradation. *Chemosphere* **2019**, *229*, 112–124. [CrossRef]
10. Chen, X.; Jia, S.; Ding, N.; Shi, J.; Wang, Z. Capture of aromatic organic pollutants by hexagonal boron nitride nanosheets: Density functional theoretical and molecular dynamic investigation. *Environ. Sci. Nano* **2016**, *3*, 1493–1503. [CrossRef]
11. Chang, H.; Chao, Y.; Pang, J.; Li, H.; Lu, L.; He, M.; Chen, G.; Zhu, W.; Li, H. Advanced Overlap Adsorption Model of Few-Layer Boron Nitride for Aromatic Organic Pollutants. *Ind. Eng. Chem. Res.* **2018**, *57*, 4045–4051. [CrossRef]
12. Li, Q.; Yang, T.; Yang, Q.; Wang, F.; Chou, K.-C.; Hou, X. Porous hexagonal boron nitride whiskers fabricated at low temperature for effective removal of organic pollutants from water. *Ceram. Int.* **2016**, *42*, 8754–8762. [CrossRef]
13. Yoosefian, M.; Etminan, N.; Moghani, M.Z.; Mirzaei, S.; Abbasi, S. The role of boron nitride nanotube as a new chemical sensor and potential reservoir for hydrogen halides environmental pollutants. *Superlattices Microstruct.* **2016**, *98*, 325–331. [CrossRef]
14. dos Santos, J.R.; da Silva, E.L.; de Oliveira, O.V.; dos Santos, J.D. Theoretical study of sarin adsorption on (12,0) boron nitride nanotube doped with silicon atoms. *Chem. Phys. Lett.* **2020**, *738*, 136816. [CrossRef]
15. Wang, R.-X.; Zhang, D.-J.; Liu, C.-B. Theoretical study of adsorption of chlorinated phenol pollutants on CO-doped boron nitride nanotubes. *Acta Phys.-Chim. Sin.* **2015**, *31*, 877–884. [CrossRef]
16. Wang, R.-X.; Zhang, D.-J.; Zhu, R.-X.; Liu, C.-B. Theoretical study of the adsorption of pentachlorophenol on the pristine and Fe-doped boron nitride nanotubes. *J. Mol. Model.* **2014**, *20*, 2093. [CrossRef]
17. Ren, X.-M.; Guo, L.-H. Molecular toxicology of polybrominated diphenyl ethers: Nuclear hormone receptor mediated pathways. *Environ. Sci. Process. Impacts* **2013**, *15*, 702–708. [CrossRef]

18. Wang, R.; Zhang, D.; Liu, C. DFT study of the adsorption of 2,3,7,8-tetrachlorodibenzo-p-dioxin on pristine and Ni-doped boron nitride nanotubes. *Chemosphere* **2017**, *168*, 18–24. [[CrossRef](#)]
19. Mahdavian, L. Computational Investigation of 2,3,7,8-Tetrachlorodibenzo-Para-Dioxin (TCDD) Adsorption on Boron Nitride-Nanotube (BNNT). *Polycycl. Aromat. Compd.* **2020**, *40*, 824–831. [[CrossRef](#)]
20. Ding, N.; Chen, X.; Wu, C.-M.L. Interactions between polybrominated diphenyl ethers and graphene surface: A DFT and MD investigation. *Environ. Sci. Nano* **2014**, *1*, 55–63. [[CrossRef](#)]
21. Wang, S.; Zhang, S.; Huang, H.; Niu, Z.; Han, W. Characterization of polybrominated diphenyl ethers (PBDEs) and hydroxylated and methoxylated PBDEs in soils and plants from an e-waste area, China. *Environ. Pollut.* **2014**, *184*, 405–413. [[CrossRef](#)] [[PubMed](#)]
22. Ishihara, S.; Labuta, J.; Van Rossom, W.; Ishikawa, D.; Minami, K.; Hill, J.P.; Ariga, K. Porphyrin-based sensor nanoarchitectonics in diverse physical detection modes. *Phys. Chem. Chem. Phys.* **2014**, *16*, 9713–9746. [[CrossRef](#)]
23. Wong, R.C.; Lo, P.-C.; Ng, D. Stimuli responsive phthalocyanine-based fluorescent probes and photosensitizers. *Coord. Chem. Rev.* **2019**, *379*, 30–46. [[CrossRef](#)]
24. Reardon, K.F.; Zhong, Z.; Lear, K.L. Environmental Applications of Photoluminescence-Based Biosensors. In *Optical Sensor Systems in Biotechnology*; Rao, G., Ed.; Springer: Berlin/Heidelberg, Germany, 2009; pp. 143–157.
25. Lever, A.B.P. The Phthalocyanines. In *Advances in Inorganic Chemistry and Radiochemistry*; Emeléus, H.J., Sharpe, A.G., Eds.; Academic Press: Cambridge, MA, USA, 1965; Volume 7, pp. 27–114.
26. Zhou, R.; Josse, F.; Göpel, W.; Öztürk, Z.Z.; Bekaroğlu, Ö. Phthalocyanines as Sensitive Materials for Chemical Sensors. *Appl. Organomet. Chem.* **1996**, *10*, 557–577. [[CrossRef](#)]
27. Guillaud, G.; Simon, J.; Germain, J.P. Metallophthalocyanines: Gas sensors, resistors and field effect transistors. In memory of Christine Maleysson. *Coord. Chem. Rev.* **1998**, *178–180*, 1433–1484. [[CrossRef](#)]
28. Lever, A.B.P. The Phthalocyanines—Molecules of Enduring Value; A Two-dimensional Analysis of Redox Potentials. *J. Porphyr. Phthalocyanines* **1999**, *3*, 488–499. [[CrossRef](#)]
29. Armstrong, N.R. Phthalocyanines and porphyrins as materials. *J. Porphyr. Phthalocyanines* **2000**, *4*, 414–417. [[CrossRef](#)]
30. de Saja, J.; Rodríguez-Méndez, M. Sensors based on double-decker rare earth phthalocyanines. *Adv. Colloid Interface Sci.* **2005**, *116*, 1–11. [[CrossRef](#)]
31. Zhu, P.; Wang, Y.; Ma, P.; Song, F.; Han, X.; Yao, S.; Yang, C. Highly ordered sandwich-type (phthalocyaninato)(porphyrinato) europium double-decker nanotubes and room temperature NO<sub>2</sub> sensitive properties. *Dalton Trans.* **2017**, *46*, 1531–1538. [[CrossRef](#)]
32. Collins, G.; Schiffrin, D. The electrochromic properties of lutetium and other phthalocyanines. *J. Electroanal. Chem. Interfacial Electrochem.* **1982**, *139*, 335–369. [[CrossRef](#)]
33. Konami, H.; Hatano, M.; Kobayashi, N.; Osa, T. Redox potentials of a series of lanthanide-bisphthalocyanine sandwich complexes. *Chem. Phys. Lett.* **1990**, *165*, 397–400. [[CrossRef](#)]
34. Weijing, D.; Weihong, Z.; Xiaodong, Z.; Baofeng, Z.; Lei, C.; Laizhi, S.; Shuangxia, Y.; Haibin, G.; Guanyi, C.; Liang, Z.; et al. The application of DFT in catalysis and adsorption reaction system. *Energy Procedia* **2018**, *152*, 997–1002. [[CrossRef](#)]
35. Rodrigues, N.M.; Daniel, C.R.A.; Edna da Silva, M.R.; da Costa, N.B., Jr.; Gimenez, I.D.F.; Freire, R.O. Lanthanide organic frameworks geometry prediction accuracies of quantum chemical calculations. *J. Mol. Struct.* **2019**, *1184*, 310–315. [[CrossRef](#)]
36. Dutra, J.D.L.; Filho, M.A.M.; Rocha, G.B.; Freire, R.O.; Simas, A.M.; Stewart, J.J.P. Sparkle/PM7 Lanthanide Parameters for the Modeling of Complexes and Materials. *J. Chem. Theory Comput.* **2013**, *9*, 3333–3341. [[CrossRef](#)] [[PubMed](#)]
37. Kadish, K.; Guillard, R.; Smith, K.M. *The Porphyrin Handbook: Phthalocyanines: Spectroscopic and Electrochemical Characterization*; Academic Press: Cambridge, MA, USA, 2012.
38. Trogen, G.-B.; Annala, A.; Eriksson, J.; Kontteli, M.; Meriluoto, J.; Sethson, I.; Zdunek, J.; Edlund, U. Conformational Studies of Microcystin-LR Using NMR Spectroscopy and Molecular Dynamics Calculations. *Biochemistry* **1996**, *35*, 3197–3205. [[CrossRef](#)]
39. Stewart, J.J.P. Optimization of parameters for semiempirical methods VI: More modifications to the NDDO approximations and re-optimization of parameters. *J. Mol. Model.* **2012**, *19*, 1–32. [[CrossRef](#)]
40. Johnson, E.R.; Keinan, S.; Mori-Sánchez, P.; Contreras-García, J.; Cohen, A.J.; Yang, W. Revealing Noncovalent Interactions. *J. Am. Chem. Soc.* **2010**, *132*, 6498–6506. [[CrossRef](#)]
41. Contreras-García, J.; Johnson, E.R.; Keinan, S.; Chaudret, R.; Piquemal, J.-P.; Beratan, D.; Yang, W. NCIPLOT: A Program for Plotting Noncovalent Interaction Regions. *J. Chem. Theory Comput.* **2011**, *7*, 625–632. [[CrossRef](#)]
42. Allouche, A.-R. Gabedit—A graphical user interface for computational chemistry softwares. *J. Comput. Chem.* **2011**, *32*, 174–182. [[CrossRef](#)]
43. Neese, F. The ORCA program system. *Wiley Interdiscip. Rev. Comput. Mol. Sci.* **2012**, *2*, 73–78. [[CrossRef](#)]
44. Neese, F. Software update: The ORCA program system, version 4.0. *Wiley Interdiscip. Rev. Comput. Mol. Sci.* **2018**, *8*, e1327. [[CrossRef](#)]
45. Neese, F.; Wennmohs, F.; Becker, U.; Riplinger, C. The ORCA quantum chemistry program package. *J. Chem. Phys.* **2020**, *152*, 224108. [[CrossRef](#)] [[PubMed](#)]
46. Koopmans, T. Über die Zuordnung von Wellenfunktionen und Eigenwerten zu den Einzelnen Elektronen Eines Atoms. *Physica* **1934**, *1*, 104–113. [[CrossRef](#)]
47. Geerlings, P.; De Proft, A.F.; Langenaeker, W. Conceptual Density Functional Theory. *Chem. Rev.* **2003**, *103*, 1793–1874. [[CrossRef](#)] [[PubMed](#)]
48. Parr, R.G.; Pearson, R.G. Absolute hardness: Companion parameter to absolute electronegativity. *J. Am. Chem. Soc.* **1983**, *105*, 7512–7516. [[CrossRef](#)]

49. Pearson, R.G.; Songstad, J. Application of the Principle of Hard and Soft Acids and Bases to Organic Chemistry. *J. Am. Chem. Soc.* **1967**, *89*, 1827–1836. [[CrossRef](#)]
50. Pearson, R.G. Hard and Soft Acids and Bases. *J. Am. Chem. Soc.* **1963**, *85*, 3533–3539. [[CrossRef](#)]
51. Parr, R.G. Density functional theory of atoms and molecules. In *Horizons of Quantum Chemistry*; Springer: Berlin/Heidelberg, Germany, 1980; pp. 5–15.
52. Kitagawa, Y.; Kawakami, T.; Yamanaka, S.; Okumura, M. DFT and DFT-D studies on molecular structure of double-decker phthalocyaninato-terbium(III) complex. *Mol. Phys.* **2014**, *112*, 995–1001. [[CrossRef](#)]
53. Gottfried, J.M. Surface chemistry of porphyrins and phthalocyanines. *Surf. Sci. Rep.* **2015**, *70*, 259–379. [[CrossRef](#)]
54. Joon, N.K.; Barnsley, J.E.; Ding, R.; Lee, S.; Latonen, R.-M.; Bobacka, J.; Gordon, K.C.; Ogawa, T.; Lisak, G. Silver(I)-selective electrodes based on rare earth element double-decker porphyrins. *Sens. Actuators B Chem.* **2020**, *305*, 127311. [[CrossRef](#)]
55. Krasnov, P.O.; Basova, T.V.; Hassan, A. Interaction of metal phthalocyanines with carbon zigzag and armchair nanotubes with different diameters. *Appl. Surf. Sci.* **2018**, *457*, 235–240. [[CrossRef](#)]
56. Dyrda, G.; Zakrzyk, M.; Broda, M.A.; Pędziński, T.; Mele, G.; Słota, R. Hydrogen Bond-Mediated Conjugates Involving Lanthanide Diphthalocyanines and Trifluoroacetic Acid (Lnpc(2)@TFA): Structure, Photoactivity, and Stability. *Molecules* **2020**, *25*, 3638. [[CrossRef](#)] [[PubMed](#)]
57. Komeda, T.; Katoh, K.; Yamashita, M. Double-decker phthalocyanine complex: Scanning tunneling microscopy study of film formation and spin properties. *Prog. Surf. Sci.* **2014**, *89*, 127–160. [[CrossRef](#)]
58. Katoh, K.; Isshiki, H.; Komeda, T.; Yamashita, M. Molecular Spintronics Based on Single-Molecule Magnets Composed of Multiple-Decker Phthalocyaninato Terbium(III) Complex. *Chem.-Asian J.* **2012**, *7*, 1154–1169. [[CrossRef](#)]
59. Serrano, G.; Velez-Fort, E.; Cimatti, I.; Cortigiani, B.; Malavolti, L.; Betto, D.; Ouerghi, A.; Brookes, N.B.; Mannini, M.; Sessoli, R. Magnetic bistability of a TbPc<sub>2</sub> submonolayer on a graphene/SiC(0001) conductive electrode. *Nanoscale* **2018**, *10*, 2715–2720. [[CrossRef](#)]
60. Candini, A.; Klar, D.; Marocchi, S.; Corradini, V.; Biagi, R.; De Renzi, V.; DEL Pennino, U.; Troiani, F.; Bellini, V.; Klyatskaya, S.; et al. Spin-communication channels between Ln(III) bis-phthalocyanines molecular nanomagnets and a magnetic substrate. *Sci. Rep.* **2016**, *6*, 21740. [[CrossRef](#)]
61. Studniarek, M.; Wäckerlin, C.; Singha, A.; Baltic, R.; Diller, K.; Donati, F.; Rusponi, S.; Brune, H.; Lan, Y.; Klyatskaya, S.; et al. Understanding the Superior Stability of Single-Molecule Magnets on an Oxide Film. *Adv. Sci.* **2019**, *6*, 1901736. [[CrossRef](#)]
62. Martínez-Díaz, M.V.; de la Torre, G.; Torres, T. Lighting porphyrins and phthalocyanines for molecular photovoltaics. *Chem. Commun.* **2010**, *46*, 7090–7108. [[CrossRef](#)]
63. Nagaraj, G.; Mohammed, M.K.A.; Abdulzahraa, H.G.; Sasikumar, P.; Karthikeyan, S.; Tamilarasu, S. Effects of the surface of solar-light photocatalytic activity of Ag-doped TiO<sub>2</sub> nanohybrid material prepared with a novel approach. *Appl. Phys. A* **2021**, *127*, 269. [[CrossRef](#)]
64. Colombelli, A.; Serri, M.; Mannini, M.; Rella, R.; Manera, M.G. Volatile Organic Compounds sensing properties of TbPc<sub>2</sub> thin films: Towards a plasmon-enhanced opto-chemical sensor. *Sens. Actuators B Chem.* **2017**, *253*, 266–274. [[CrossRef](#)]
65. Blase, X.; Rubio, A.; Louie, S.G.; Cohen, M.L. Stability and Band Gap Constancy of Boron Nitride Nanotubes. *Eur. Lett.* **1994**, *28*, 335–340. [[CrossRef](#)]
66. Chou, Y.-M.; Wang, H.-W.; Lin, Y.-J.; Chen, W.-H.; Wang, B.-C. Infinite single-walled boron-nitride nanotubes studies by LGTO-PBC-DFT method. *Diam. Relat. Mater.* **2009**, *18*, 351–354. [[CrossRef](#)]
67. Lauret, J.S.; Arenal, R.; Ducastelle, F.; Loiseau, A.; Cau, M.; Attal-Tretout, B.; Rosencher, E.; Goux-Capes, L. Optical Transitions in Single-Wall Boron Nitride Nanotubes. *Phys. Rev. Lett.* **2005**, *94*, 037405. [[CrossRef](#)] [[PubMed](#)]
68. Xiang, H.; Yang, J.; Hou, J.; Zhu, Q. First-principles study of small-radius single-walled BN nanotubes. *Phys. Rev. B* **2003**, *68*, 035427. [[CrossRef](#)]
69. Suzuki, A.; Oku, T. Effects of central metal on electronic structure, magnetic properties, infrared and Raman spectra of double-decker phthalocyanine. *Appl. Surf. Sci.* **2016**, *380*, 127–134. [[CrossRef](#)]
70. Bottari, G.; de la Torre, G.; Guldi, D.M.; Torres, T. Covalent and Noncovalent Phthalocyanine–Carbon Nanostructure Systems: Synthesis, Photoinduced Electron Transfer, and Application to Molecular Photovoltaics. *Chem. Rev.* **2010**, *110*, 6768–6816. [[CrossRef](#)]